applied sciences

MDPI

Article

Effects of an Optimized Adhesive Distribution on Stresses and Strains in the Rotor and Magnets of a Surface Permanent-Magnet Synchronous Electric Motor

Davide Oldoini [1,*], Saverio Giulio Barbieri [1,*], Giampaolo Devito [1], Matteo Giacopini [1] and Michael Galea [2]

[1] Engineering Department "Enzo Ferrari", University of Modena and Reggio Emilia, 41125 Modena, Italy; giampaolo.devito@unimore.it (G.D.); matteo.giacopini@unimore.it (M.G.)
[2] Faculty of Engineering, University of Malta, 2080 Msida, Malta; michael.d.galea@um.edu.mt
* Correspondence: davide.oldoini@unimore.it (D.O.); saveriogiulio.barbieri@unimore.it (S.G.B.); Tel.: +39-059-2056112 (S.G.B.)

Abstract

It is well-established in the literature that surface-mounted permanent-magnet synchronous motors (SPMSMs) have a high torque density due to an elevated interaction between magnetic flux and windings. For this reason, SPMSMs are extensively studied. This paper investigated the mechanical interactions and strains that develop in the main components of the rotor of an SPMSM, with particular focus on the behavior of the adhesive layer used for magnet bonding. An iterative methodology was proposed to improve both the amount and distribution of the adhesive to reduce stress, from 182 to 9 MPa, and deformation, from 0.182 to 0.008 mm, in critical components such as permanent magnets (PMs). SPMSM rotors are particularly sensitive to centrifugal forces, which tend to expel the PMs radially toward the stator. This effect leads to deformations in the rotor, PMs, and adhesive layer, resulting in a reduction of 16% from the original airgap without adhesive and in the generation of stresses that must remain within acceptable limits, stresses which go beyond 170 MPa in the layout without adhesive. Several fastening configurations of the PMs were analyzed, each incorporating a mechanical retaining element, primarily for safety purposes, combined with different adhesive distribution strategies.

Keywords: surface permanent-magnet synchronous motor (SPMSM); adhesive; structural analysis; finite element analysis; optimization

Academic Editor: Ephraim Suhir

Received: 17 November 2025
Revised: 9 December 2025
Accepted: 12 December 2025
Published: 16 December 2025

Citation: Oldoini, D.; Barbieri, S.G.; Devito, G.; Giacopini, M.; Galea, M. Effects of an Optimized Adhesive Distribution on Stresses and Strains in the Rotor and Magnets of a Surface Permanent-Magnet Synchronous Electric Motor. *Appl. Sci.* **2025**, *15*, 13179. https://doi.org/10.3390/app152413179

1. Introduction

In recent years, optimizations and structural Finite Element Method (FEM) analyses in the field of electric motors (EMs) have progressed rapidly [1]. In [1] the authors investigate a wound-rotor electrical machine by coupling structural and thermal analyses to assess the potential for performance enhancement under realistic operating conditions. Several studies have focused on optimizing permanent-magnet (PM) shape, distribution, and geometric tailoring [2–6]. In [2], a multi-objective, multi-physics optimization algorithm is proposed for a PM-assisted Synchronous Reluctance Machine (SynRM), where electromagnetic and mechanical aspects are simultaneously optimized, contrary to traditional approaches where the two domains are often treated separately. In [3], another multi-physics, multi-objective optimization is presented for a V-shape IPMSM to maximize torque. In this case, electromagnetic, structural, and thermal analyses are carried out sequentially rather than fully

coupled. In [4], the authors introduce a hybrid shape-optimization methodology combining parametric optimization (typically applied to PMs) with topology optimization (commonly applied to flux barriers), targeting the concurrent reduction in torque ripple and the maximization of torque. In [5], a consequent-pole PM (CPM) topology is proposed. This configuration can reduce rare-earth PM usage by up to 50%, thanks to a continuous magnetization layout in which adjacent poles share the same orientation. Numerical optimizations are performed to mitigate cogging torque and torque ripple, critical issues for this topology. In [6], another CPM motor design with flared PMs is investigated via FEM to assess technological feasibility. Parametric optimizations are carried out to improve performance and validate the manufacturability of the proposed geometry.

Other studies investigate strategies for reducing PM mass and rare-earth material usage [7–10]. In [7], a comprehensive review of hybrid rare-earth and full rare-earth PM machines is presented, outlining guidelines to overcome current limitations and reduce production costs while preserving performance. In [8], several approaches are proposed to reduce rare-earth PM usage by introducing ferrite magnets, supported by a multistep, iterative FEM-based design workflow. A dedicated magnet-design methodology for hybrid low-rare-earth (HLRE) machines is also introduced. In [9], a flux-reversal PM motor topology is proposed with the explicit goal of minimizing rare-earth dependency. The motor operates as a PM-assisted reluctance machine, combining magnetic saliency and reduced PM material. In [10], the authors investigate the use of "banana-shaped" PMs to reduce rare-earth content while maintaining torque performance. Although more efficient at equal mass, the geometry is harder to manufacture. Alternative magnetization patterns are therefore proposed to simplify large-scale production.

The SPMSM analyzed in this work has been previously optimized from an electromagnetic standpoint [11]. Therefore, the electromagnetic behavior of the baseline machine (such as flux distribution, torque capability, and PM sizing) has been considered established and has not been revisited here. The present paper focuses exclusively on the mechanical integrity of the rotor–PM assembly, re-evaluating the electromagnetic performance only insofar as it is directly affected by the adhesive grooves and the corresponding local airgap variations. In such motors, the main structural issue is the centrifugal force, which tends to expel the PMs radially toward the stator [12]. This can lead to excessive stress, deformation, or even PM detachment, as highlighted in [13], compromising both structural integrity and motor functionality [14–16]. Centrifugal force acts only during rotation and becomes particularly critical at high speeds. Its intensity is proportional to the mass of the PM, its radial position, and the square of the angular velocity, as given by the following equation:

$$F = m * \omega^2 * r \tag{1}$$

where m is the mass of the PM, ω is the angular velocity, and r is the distance from the rotation center. SPMSMs are especially sensitive to centrifugal loads for two main reasons. First, PMs are placed farther from the rotation center than in other configurations (e.g., IPMSMs). Second, PMs are directly exposed to the stator, with no structural support between them. The larger radius implies greater centrifugal loads on SPMSMs compared to IPMSMs. Additionally, the absence of supporting structural material behind the PMs increases their deformability and hampers uniform stress distribution. The differences between IPMSMs and SPMSMs extend well beyond these aspects, as detailed in [17]. Further complications arise from the PM manufacturing process, particularly due to the sintering stage [18–20]. Sintered Neodymium–Iron–Boron (Nd-Fe-B) PMs have relatively poor tensile and flexural strength [21]. Therefore, it is crucial to limit stress concentrations in the PMs. To mitigate such issues, several approaches have been proposed in the literature, including carbon or glass fiber sleeves [22] and diamagnetic metallic alloys [23]. Carbon sleeve-based solutions

are often hybrid systems, combining the sleeve with an adhesive layer. These systems reduce both deformations and peak stresses on PMs and the rotor, ensuring more effective mechanical stress distribution [24]. However, introducing a carbon or metal sleeve increases the airgap between the rotor and stator, leading to non-negligible performance losses [25]. To overcome this drawback, an innovative layout has been proposed in which radial PM retention is achieved solely through mechanical teeth and one or more adhesive layers. Another key contribution of the present work is a systematic optimization of the adhesive distribution between the PM and the rotor, aimed at minimizing the adhesive volume and its magnetic impact while preserving mechanical retention. Conventional solutions based on continuous carbon or metal sleeves inevitably increase the effective airgap and reduce electromagnetic performance. On the contrary, the present approach explores selective, controlled adhesive patterns and quantities that provide required mechanical safety margins with a smaller magnetic penalty. Characteristics such as torque density, efficiency, and ease of control, which are particularly important in the aviation industry, make SPMSMs highly desirable, especially in fixed-speed applications, such as starter generators (SGs). Therefore, these aspects have been considered as the ones that led to the choice of this type of EM over all other options available both on the market and in the literature.

The present study focuses on improving the distribution of adhesive between PMs and the rotor. Four configurations have been analyzed, differing in adhesive quantity and placement, from no adhesive to full-surface bonding of the PM back face. The complete model of the motor is shown in Figure 1a, together with a detailed view of the rotor–PM assembly, Figure 1b. In Figure 1b, which represents one magnetic pole of the electric machine, both a portion of the rotor and a full PM have been included. By observing the contact area between the rotor and the PM, two radial retention teeth might be seen on the sides of the PM. Their shape is commonly referred to as dovetail. This feature constitutes one of the two elements responsible for radially restraining the PM. The regions highlighted in yellow indicate the areas where the adhesive should be applied, namely, the other element cooperating with the mechanical dovetail in ensuring the radial retention of the PM. The particular shape of the PM results from a previously conducted multi-objective optimization process. Several design constraints, and their combination, had to be satisfied accounting for both performance and environmental aspects. This optimization led to the geometry depicted in Figure 1b. The FEM approach is adopted to evaluate stress and strain on critical components. For the adhesive layer, the Cohesive Zone Model (CZM) has been employed.

The present paper is structured as follows. Section 2 describes the main applications of SPMSM. Section 3.1 presents the modeling methodology for the adhesive layer, with a focus on the CZM. Section 3.2 describes the FEM setup, including geometry, materials, and boundary conditions. Sections 4.1–4.4 analyze the results for each layout, focusing on stress, deformation, and adhesive performance. Finally, Section 5 summarizes the key findings and outlines the trade-offs between mechanical robustness and material efficiency.

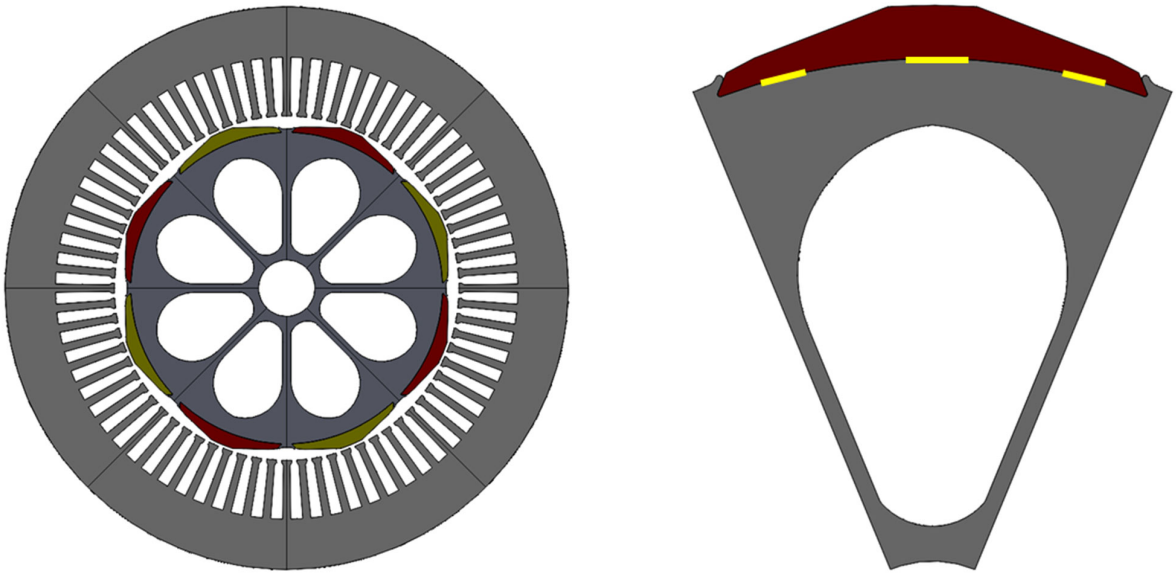

(a) (b)

Figure 1. Representation of the EM: (**a**) the complete EM, (**b**) a detailed view of the magnetic pole. It is possible to observe the mechanical teeth needed to radially hold the PM.

2. SPMSM: Main Applications

SPMSMs are widely adopted across several industrial and transportation sectors due to a combination of technical attributes that define their engineering value. Their high torque and power density, efficient electromagnetic behavior, compact construction, and excellent dynamic response make them attractive whenever performance, size, and controllability are critical design drivers. These advantages primarily derive from the placement of PMs on the rotor surface, which maximizes the effective airgap flux and enhances the magnetic coupling with the stator windings. Moreover, the absence of rotor excitation windings eliminates brushes and slip rings, reducing maintenance requirements and improving long-term reliability. Also, SPMSMs exhibit high efficiency over a wide speed range because no field current is required to establish rotor flux, and magnetic losses remain relatively low. From a dynamic perspective, their capability to generate rapid torque transients and follow advanced control algorithms—such as field-oriented control (FOC) or direct torque control (DTC)—makes them suitable for applications demanding precise position or speed regulation and fast response. Although SPMSMs offer several advantages, they also impose specific design constraints. The surface-mounted PMs are more exposed to mechanical loads, thermal degradation, and the risk of partial demagnetization. For this reason, suitable retention strategies, such as mechanical teeth, adhesive bonding, or protective sleeves, must be adopted to ensure safe operation, especially in high-speed applications. SPMSMs may also exhibit significant cogging torque and torque ripple, which require careful electromagnetic design involving PM shaping, optimized slot-pole combinations, winding layout strategies, or current profiling. Finally, the use of rare-earth magnetic materials introduces cost and sustainability considerations that often motivate design approaches aimed at minimizing PM volume or adopting alternative PM arrangements. These characteristics explain why SPMSMs are used in a range of practical applications, where their strengths align with the specific technical requirements of each sector. The main application domains are summarized below.

Automotive: SPMSMs are extensively employed in electric traction systems, particularly for light-duty vehicles and hybrid architectures. Their high torque density enables compact motor designs that fit within tight packaging constraints, while their high efficiency contributes directly to extending vehicle range. SPMSMs also provide excellent control-

lability and fast torque response, which are essential for vehicle dynamics, regenerative braking, and overall drivability. The mechanical simplicity of the surface-mounted rotor reduces rotating inertia and manufacturing complexity, advantages that are particularly valuable in electric mobility applications [26].

Aerospace: In the aerospace sector, SPMSMs are used in high-speed starter generator (SG) units and other onboard electromechanical systems. Their high power density and favorable mass-to-performance ratio allow the development of compact and lightweight machines that meet stringent aviation or military requirements. However, aerospace environments impose severe mechanical and thermal loads. High rotational speeds amplify centrifugal forces acting on PMs, making their retention (through mechanical teeth, adhesive layers, or sleeves) a critical aspect of rotor design. Thermal management is also essential to prevent demagnetization and ensure long-term reliability. These challenges make SPMSMs well-suited for aerospace applications, provided that adequate structural design measures are implemented [27].

Electric Energy Generation: SPMSMs are also used in electrical generation systems, especially in low-speed or direct-drive configurations such as wind turbines. In these systems, surface-mounted PM rotors offer low cogging torque, favorable thermal characteristics, and high surface power density, making them efficient in capturing mechanical energy at low rotational speeds. Variants such as Halbach arrays or eccentric PM arrangements are frequently studied to further improve flux distribution and maximize output under low-speed conditions. Their simple mechanical architecture and high efficiency make SPMSMs a strong candidate for renewable energy systems and distributed generation [28].

Robotics and Industrial Automation: SPMSMs are widely adopted in robotics, precision servo systems, machine tools, and industrial automation. Their high dynamic responsiveness, excellent torque linearity, and compatibility with advanced control schemes enable precise and rapid motion execution. The compactness of the SMPSMs and low maintenance requirements support integration into articulated robotic arms, CNC stages, and high-performance actuation systems. These characteristics make SPMSMs a reference solution for motion control applications demanding high accuracy, repeatability, and reliability [29].

Compressors and Pumps: In compact, high-efficiency electric pumps and compressors, SPMSMs allow the development of machines capable of delivering high power density within restricted volumes. Their ability to maintain good performance over a wide operating range, combined with fast response achieved through vector control, makes them suitable for automotive HVAC systems, industrial compressors, refrigeration units, and high-speed pumps. The reduced mechanical complexity of the rotor contributes to greater reliability, especially in continuous-operation environments [30].

3. Modeling Methods and Material Property Definition

3.1. Cohesive Zone Model

The methodology adopted to model the mechanical behavior of the adhesive was the CZM. By adopting this approach, the adhesive layer was represented by three-dimensional cohesive elements, which can accurately model both the initiation and propagation of damage at the adhesive interface [31]. Their mechanical response was defined by a bilinear law, a common practice for brittle adhesives [32]. This law, known as the traction–separation law, comprises two distinct segments. First, the linear and increasing segment represents the elastic response of the adhesive. Second, the other segment, also linear but decreasing, describes the progressive degradation of stiffness as damage accumulates. Figure 2 shows the curve in greater detail.

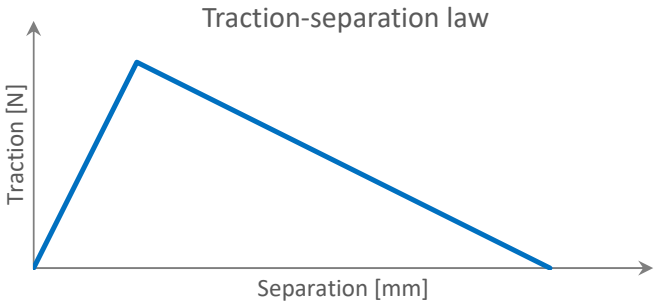

Figure 2. Representation of the curve characterizing the bilinear traction–separation law of the modeled adhesive.

Damage initiates when a stress threshold is exceeded. This threshold is based on the characteristic strengths of the adhesive, in both tension and shear. The combination of these stresses is evaluated using a quadratic criterion that determines the onset of cohesive failure, according to the following equation, implemented within the OptiStruct FEM solver [32]:

$$\left(\frac{\sigma_I}{\max(\sigma_I)}\right)^2 + \left(\frac{\sigma_{II}}{\max(\sigma_{II})}\right)^2 + \left(\frac{\sigma_{III}}{\max(\sigma_{III})}\right)^2 = 1 \quad (2)$$

where σ_I, σ_{II}, and σ_{III} represent the current stress for each failure mode, and max (σ_I), max (σ_{II}), max (σ_{III}) are the corresponding adhesive strength limits. Once this threshold is surpassed, stiffness decreases through a phenomenon known as softening [33]. Damage propagation is governed by the energy per unit area that the cohesive element can absorb. This is defined for the three main fracture modes: opening slip, in-plane shear, and out-of-plane shear. The following equation, always implemented within the OptiStruct FEM solver, governs the process [32]:

$$\left(\frac{G_I}{G_{Ic}}\right)^{\alpha} + \left(\frac{G_{II}}{G_{IIc}}\right)^{\alpha} + \left(\frac{G_{III}}{G_{IIIc}}\right)^{\alpha} = \left(\frac{G}{G_c}\right)^{\alpha} \quad (3)$$

where G_{Ic}, G_{IIc}, and G_{IIIc} represent the critical energy values for failure in modes I, II, and III. G_c is the total critical energy, while G_I, G_{II}, and G_{III} are the energies under the traction–separation curve up to the current step, and G is the total absorbed energy at that step. This equation governs the ability of the interface to maintain continuity during the softening phase. When the absorbed energy reaches the critical energy defined by the damage evolution law (Equation (3)), the cohesive element loses its load-bearing capacity. Figure 3 shows in detail fracture modes I, II, and III.

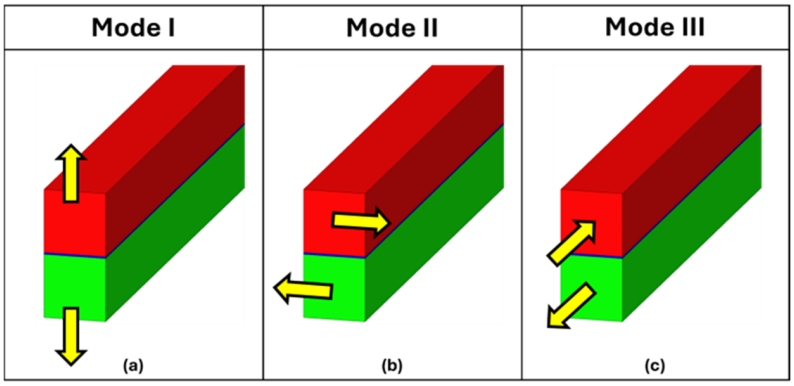

Figure 3. Simplified representation of the three modes of adhesive fracture: (**a**) opening slip, (**b**) in-plane shear, and (**c**) out-of-plane shear.

In this specific case, failure is expected to occur predominantly in mode I, the opening mode, given the adhesive configuration and the loading direction. Adhesive fractures can develop in two distinct regions. The first one, known as adhesive or interfacial failure, occurs at the interface between the adherend and the adhesive, typically resulting from inadequate surface preparation, contamination, or poor chemical compatibility. The second one, referred to as cohesive failure or cohesive fracture, arises within the adhesive itself and may be caused by low intrinsic material strength, excessive stress, or incomplete curing. In this situation, the fracture propagates through the adhesive rather than along the interface. Mixed-mode failures, involving both interfacial and cohesive mechanisms, can also occur.

The complete set of mechanical properties required for the constitutive modeling of the selected adhesive Permabond ES 5516 is neither provided by the manufacturer nor available in the literature. Only partial information is publicly reported, which is insufficient to define the full nonlinear stress–strain behavior, stiffness parameters, and failure limits needed for FE-based stress analysis. To avoid resorting to arbitrary assumptions, a surrogate adhesive with experimentally characterized parameters has been selected. Among the structural adhesives for which full mechanical characterization is available, Araldite AV138 is one of the adhesives reported in the literature with a complete set of parameters derived from systematic experimental campaigns [32,34]. Moreover, AV138 and ES 5516 share key features relevant to the present analysis, namely high stiffness and brittle behavior, making AV138 a suitable first-order proxy for modeling purposes. The use of a surrogate material is therefore not intended to represent ES 5516 exactly, but rather to provide a physically consistent baseline model in the absence of reliable data. This approximation, its implications, and its limitations are explicitly acknowledged, and the authors are currently performing the experimental characterization of ES 5516 to refine the material model in future work. The parameters used are reported in Table 1.

Table 1. List of parameters found in the bibliography necessary for modeling the Araldite AV138 adhesive.

Parameter	Unit	Value
Young's Modulus, E	[GPa]	4.89 ± 0.81
Poisson's Ratio, ν	[-]	0.33
Tensile Failure Strength, σ_f	[MPa]	39.45 ± 3.18
Shear Modulus, G	[GPa]	1.56 ± 0.01
Shear Failure Strength, τ_f	[MPa]	30.20 ± 0.40
Toughness in Tension, G_n^c	[N/mm]	0.20
Toughness in Shear, G_s^c	[N/mm]	0.38

3.2. FEM Modeling

FEM with 3D cohesive elements has been selected. It enables local stress and strain resolution and allows direct implementation of cohesive laws for damage initiation and propagation capabilities. Lumped analytical models could not provide similar results when dealing with adhesive-layer fracture mechanics and localized stress concentrations. Analytical models remain valuable for preliminary electromagnetic or structural estimations. However, they are inherently limited when detailed evaluation of the PM–rotor interface is required.

The FEM models have been developed based on the geometric and functional specifications of the EM under investigation. The analyzed machine is an SPMSM designed to operate as an SG in the aerospace sector. In this dual-function configuration, the device starts the jet engines and later acts as a generator, converting mechanical power into electric power to supply onboard systems [35]. The main technical specifications of the SG are reported in Table 2.

Table 2. List of the main characteristic parameters of the starter generator.

Parameter	Unit	Value
Rated Power, P_N	[kW]	30
Torque, T_N	[Nm]	28.9
Rated Speed, ω_N	[rpm]	10,000
Rotor Inner Diameter, φ_{RI}	[mm]	20.00
Rotor Outer Diameter, φ_{RE}	[mm]	120.27
Airgap, A	[mm]	1.00
Stator Inner Diameter, φ_{SE}	[mm]	122.27
Stator Outer Diameter, φ_{SE}	[mm]	200.00
Height, H	[mm]	75.00
Number of Poles, N_P	[-]	8
Number of Phases, N_F	[-]	3
Stator Slots, N_S	[-]	54
Efficiency, η	[-]	98.2%
Line current	[A]	46.6
Line–Line voltage	[V]	383.5

The complete machine, comprising the stator, rotor (NO20 steel), and PMs (sintered Nd-Fe-B N38UH), can be seen in Figure 1a. To reduce computation time without compromising result quality, a partial domain model has been adopted. By exploiting geometric symmetry, the model has been limited to an angular portion equal to half of a magnetic pole and half the original rotor height. This setup reduces the simulated domain to 1/32 of the full volume of the SG. Simulations have been run at 10,000 rpm, the maximum operating speed, which corresponds to peak centrifugal loads and represents the most critical structural condition. For further simplification, the numerical model could be reduced to a single longitudinal layer of the rotor, discretized with 3D solid elements. This modeling choice enables the generation of a significantly finer mesh within the region of interest and substantially reduces computational cost, allowing detailed resolution of local stress gradients, adhesive behavior, and cohesive-zone damage evolution. However, this simplification inherently restricts the validity of the results to the rotor mid-span. Because the model excludes the axial extremities of the machine, several three-dimensional boundary phenomena, such as end-edge stress intensification, are not captured. In high-speed SPMSMs, these edge effects can influence the stress distribution near the rotor ends. As a result, the midsection of the rotor might be representative of the entire rotor, since the rotor is largely axisymmetric and the loading is uniform. This approach is consistent with established practices in the preliminary structural evaluation of high-speed rotors, but it also highlights the need for complementary full-length or sector-based 3D models when assessing effects that are strongly influenced by axial boundaries. Figure 4 displays the section of layout 1, which lacks adhesive.

Regarding element definition, both the rotor and PM structures have been modeled using about 250,000 3D hexahedral elements with linear-elastic properties, using an element size of 0.5 mm. The mesh around the contact area between the rotor and the PM has been refined, with an element size of 0.1 mm. This should ensure a good evaluation of contact. This meshing configuration has been established based on the outcomes of a preliminary sensitivity analysis. This modeling is consistent with the design condition, where stress levels should remain well below the yield limit, avoiding plastic deformation. The adhesive, as described previously, has been modeled using 3D cohesive elements with bilinear behavior. Figure 5 shows a mesh detail in the contact zone while Table 3 summarizes the material parameters used for the rotor and PMs.

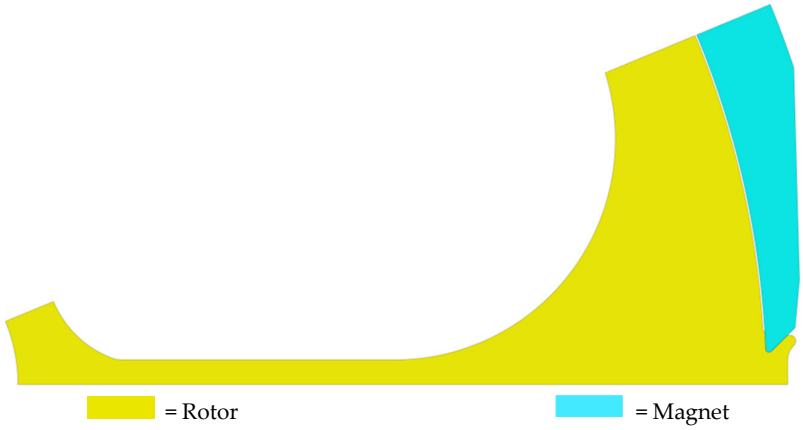

Figure 4. Top view of the first simulated layout. It can be clearly seen that the section is equal to half the magnetic pole of the rotor.

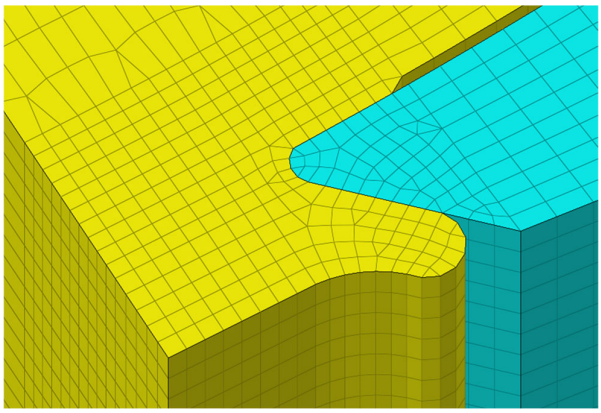

Figure 5. Representation of the direct contact area between the permanent magnet (in light blue) and the rotor (in yellow). The mesh size in this region has been reduced to properly capture the effects of contact.

Table 3. Performance of the rotor and permanent-magnet materials.

Parameter	Unit	Value
NO20 Young's Modulus, E	[GPa]	185
NO20 Poisson's Ratio, ν	[-]	0.30
NO20 Yield, σ_{SN}	[MPa]	400
NO20 Density, v	[kg/m^3]	7850
Nd-Fe-B Young's Modulus, E	[GPa]	158
Nd-Fe-B Poisson's Ratio, ν	[-]	0.24
Nd-Fe-B Yield, σ_{SN}	[MPa]	285
Nd-Fe-B Density, v	[kg/m^3]	7650

Four layouts have been developed for analysis, differing in adhesive presence and distribution:

- Layout 1—No adhesive: The PM is retained only by mechanical constraints (rotor teeth). No adhesive is used.
- Layout 2—Central groove: A 0.2 mm thick adhesive layer is applied in a 6 mm wide groove machined into the rotor, uniformly distributed axially. Nodal matching ensures proper stress transfer.
- Layout 3—Three grooves: Two additional grooves (3 mm wide, 0.2 mm deep) are added symmetrically to the central one, positioned at zones of peak PM deforma-

tion from the previous simulation. Adhesive layers are again implemented with nodal matching.

- Layout 4—Maximum bonding: The adhesive spans nearly the entire contact surface between the PM and rotor, except near the teeth. Thickness remains 0.2 mm, covering the full axial length.

From a purely magnetic standpoint, adding an adhesive layer is equivalent to introducing an additional layer of air (i.e., an airgap), unless the adhesive is ferromagnetically conductive. In this study, however, the adhesive does not exhibit such properties. Therefore, its presence might be interpreted as an additional airgap through which the magnetic flux must pass when closing the flux lines on the PM. It is common knowledge that introducing an additional airgap between the rotor and the PM in an SPMSM inevitably reduces the magnetic performance and, consequently, the torque capability of the machine. Specifically, when comparing layout 1 and 4, the first is characterized by the absence of adhesive and the entire back surface of the PM is in direct contact with the rotor. The latter is equipped with a groove for adhesive application that covers almost the entire PM back surface. In layout 4, the maximum torque decreases by approximately 3% if compared with layout 1. Layout 2 is characterized by a single adhesive groove, 6 mm wide and 0.2 mm thick. This layout shows a torque reduction of about 0.8% with respect to layout 1. Layout 3, with three adhesive grooves, exhibits a reduction of roughly 1% compared to layout 1. For simplicity, all simulations presented in this study have been performed using the FEM model of the rotor corresponding to layout 4, the configuration with the largest groove, which is shown in Figure 6d. In fact, the presence of the grooves is mechanically and structurally negligible. However, the additional airgap exists only where the grooves (and therefore the adhesive) are located, and not along the entire inner arc of the PM, as assumed in the simulations. Although using layout 4 as a reference model is magnetically non-ideal, it allows greater flexibility in positioning the adhesive layers at the various locations of interest without requiring a dedicated rotor model for each configuration. This approach significantly accelerates both the simulation setup and the generation of results. Consequently, depending on the layout under investigation, the corresponding adhesive layers are modeled within the geometry featuring the largest slot between the rotor and the PM.

An important aspect concerns the PM–tooth contact. Since the two components are not bonded in this area, relative sliding is allowed. The model considers the effects of friction by using two coefficients: the first, μ_s = 0.74, refers to static friction and the second, μ_d = 0.57, refers to dynamic friction. Sliding occurs when the tangential force exceeds the product of normal force and static friction, according to:

$$F_{TGmax} = F_N * \mu_s \tag{4}$$

where F_{TGmax} is the maximum tangential force that friction can resist, F_N is the normal force, and μ_s is the coefficient of static friction. To ensure local accuracy, a finer mesh has been generated in the contact zone, with nodal matching between the corresponding nodes of the rotor and PM.

Figure 7 shows the four different layouts previously proposed and briefly described.

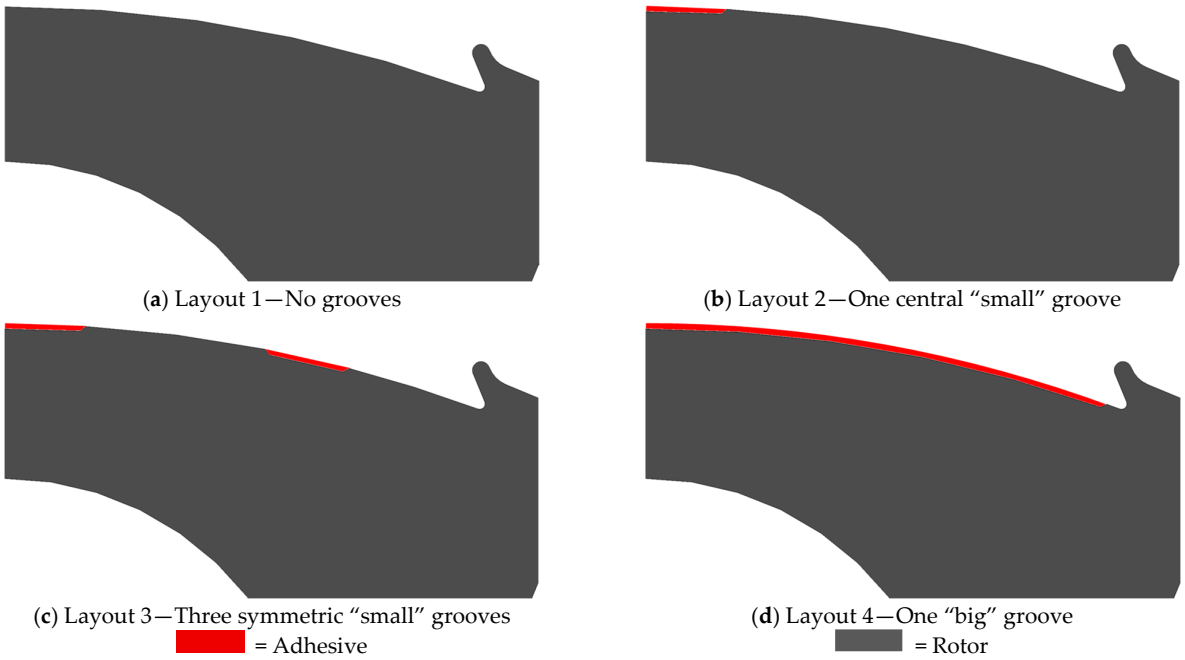

Figure 6. Representation of the four different rotor layouts. The images represent only half the magnetic pole of the rotor. Moreover, the figures show, in detail, the interface between the rotor and the permanent magnet (not present). The dovetail radial retaining tooth of the permanent magnet is also clearly visible.

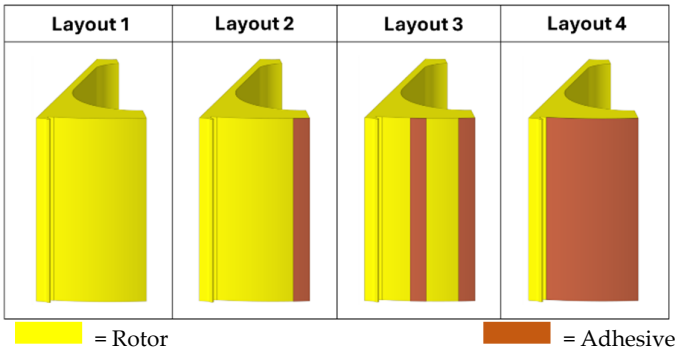

Figure 7. Representation of the different layouts simulated (**1** to **4**). Note the increase in adhesive from layout to layout, starting from one without adhesive to one where the adhesive surface is at its maximum extent.

4. Results

4.1. Layout 1

Layout 1 is the simplest configuration among the FEM models. Here, the PM is retained solely through contact with the rotor tooth, without any adhesive. As a result, the entire centrifugal load during rotation is transferred to the rotor exclusively via the retention tooth, causing high stress concentrations on both components, the rotor and PM.

By knowing the PM density, its geometry, and the rotational speed, it is possible to analytically estimate the force transmitted to the rotor. This estimation is independent of the presence or absence of adhesive, which affects only how the force is distributed over the rotor surface. Using Equation (1), the centrifugal force generated by the PM is calculated to be 1190 N. The attractive magnetic force between the rotor and the PM has been intentionally neglected. This choice ensures a conservative, safety-oriented simulation approach, producing a worst-case scenario compared to real operating conditions.

FEM analysis shows that, without adhesive, the maximum stresses occur precisely in the tooth–PM contact zone. Within the rotor, stresses are concentrated on the tooth and nearby regions, indicating localized bending. This is confirmed by the non-uniform stress distribution. In fact, peaks appear at the tooth edges, with minimum values at the center. The estimated stress levels already justify rejecting this configuration. Considering a yield strength of 400 MPa and a safety factor of 3, the 133 MPa limit is exceeded. Also, in the PM, stresses are high, with the typical bending pattern showing the maximum at the edges and minimum at the center. The peak value, around 180 MPa, surpasses the 95 MPa safety threshold, again assuming a safety factor of 3. Notably, due to the non-uniform geometry of the PM, the point of maximum stress does not align with the section of maximum bending moment. This behavior derives from the variations in the flexural strength modulus. Although the maximum moment occurs at mid-span, the most critical section is located where the combination between bending moment and resistance modulus is most unfavorable. Figure 8 illustrates the distribution of stress in the most critical zones of both components.

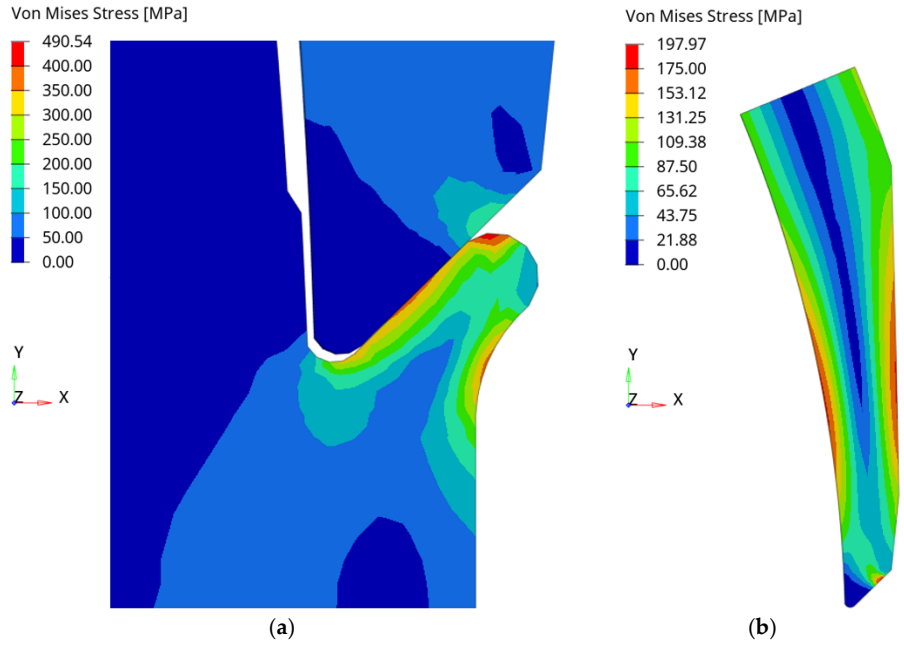

Figure 8. Von Mises stress contour plot—layout 1, (**a**) the stress distribution of the rotor tooth, (**b**) the stress distribution of the PM. Note the classic bending stress map.

Excessive deformations are also observed in both the PM and teeth. The central region of the PM experiences the greatest effects due to a higher mass concentration and its greater distance from the mechanical constraints. Given a nominal airgap of 1.00 mm, the PM deformation reduces it by 18%, reaching 0.82 mm. This can jeopardize magnetic performance, causing saturation, increased losses, and lower efficiency. Even if the mechanical strength of the tooth was adequate, the stress and deformation levels of the PM would have still made this configuration unacceptable. This case highlights the need for a multi-criteria structural assessment. A viable design should ensure that stresses remain well below the yield strength, deformations stay within functional tolerances, and the structural integrity of the rotor–PM interface is verified for both components.

4.2. Layout 2

Layout 2 is the first configuration introducing an adhesive layer between the PM and rotor. The application area has been selected based on the layout 1 results, targeting the central region of the PM, where deformations peaked. Adding adhesive here aimed at

redistributing centrifugal forces, enabling more uniform load transfer and reducing local stresses and deformations. Numerical results show a significant improvement over layout 1. Stress concentrations in the rotor teeth decrease substantially, so much so that the upper limit of the color scale had to be lowered. Although mechanical contact between the tooth and PM still exists, the main load path now passes through the adhesive, which acts as a structural bridge. The stress acting on the tooth remains mainly bending, as confirmed by the non-uniform stress distribution, but its magnitude is much lower. The maximum stress area no longer aligns with the tooth–PM interface, as shown in Figure 9.

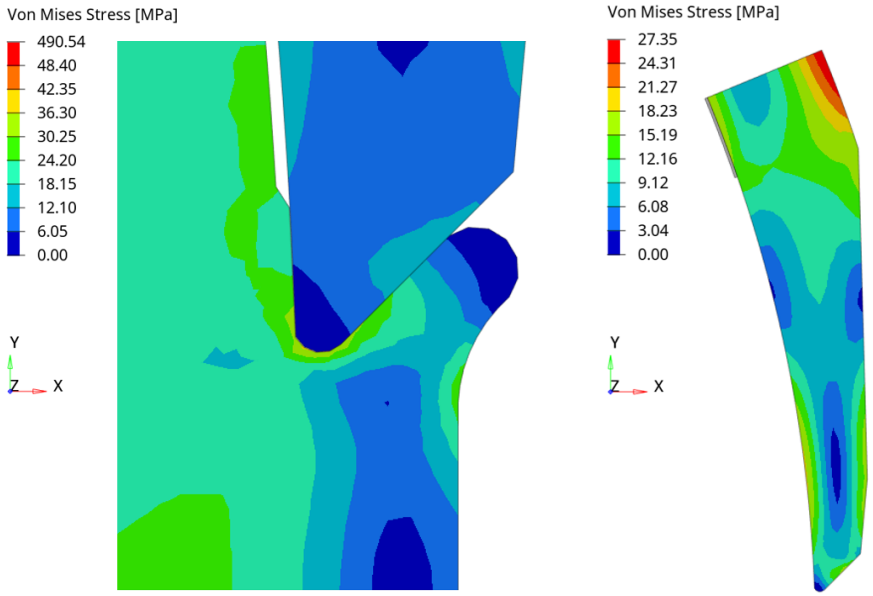

(**a**) (**b**)

Figure 9. Von Mises stress contour plot—layout 2: (**a**) the stress distribution of the rotor tooth, on a reduced scale, (**b**) the stress distribution of the PM, again on a reduced scale.

Although the Young's modulus of the adhesive is much lower than that of the rotor and PM, what matters structurally is the overall stiffness, defined by the modulus, contact area, and adhesive thickness, according to the relation:

$$k = \frac{E * A}{l} \tag{5}$$

where k is the stiffness of the component, E is the elastic modulus, A is the surface area of the adhesive, and l is its thickness. This demonstrates how, even with a low Young's modulus, a large area, and a small thickness, high stiffness can be achieved. This local stiffness allows the adhesive to effectively transfer loads. In the PM, improvement is also clear. The central adhesive introduces a third constraint point (alongside the lateral teeth), shifting from a two-point to a three-point load system, significantly reducing stress. The PM still experiences bending, but the stress levels are much lower than before, the critical region shifts toward the PM center, and the critical areas are smaller.

A key benefit of this layout is the drastic deformation drop, from 0.1668 mm (layout 1) to 0.0145 mm, over a 90% reduction. Also, the deformation peak moves from the PM center to the area between the bonded surface and the tooth contact. This suggests placing future adhesive layers where deformation peaks occur, following an iterative strategy. A critical limitation concerns adhesive stress. The adhesive primarily operates under normal loading. These stresses can be estimated conservatively, ignoring the rotor tooth contact, via the following equation:

$$\sigma_N = \frac{F}{A} \tag{6}$$

where σ_N is the normal stress, F is the centrifugal force, and A is the effective bonded surface area.

Despite low deformation, the limited bonded area results in stress between 6 and 8 MPa, with edge peaks from boundary effects. Given the limits of structural adhesives, their degradation at high temperature, and aerospace safety margins, these values are too high for reliable operation. Although the yield strength of AV138 is 39.5 MPa at room temperature, this degrades significantly at 120 °C. Assuming a safety factor of 10, acceptable stresses drop to 4 MPa. Hence, despite notable improvements, this layout cannot yet be deemed definitive due to adhesive performance constraints.

4.3. Layout 3

Layout 3 introduces two additional adhesive layers between the PM and rotor, placed where new PM deformation peaks occur. The goal is to reduce stress on cohesive elements, especially in areas subject to load concentration. Doubling the adhesive area should ideally halve the average stress due to the increased bonding surface. Compared to the transition from layout 1 to 2, the changes from layout 2 to 3 are less pronounced, as can be seen in Figure 10. The rotor shows localized stress reduction, mainly in the tooth area, confirming that more load paths now pass through the adhesive, further lightening the load that passes through the mechanical contact between the PM and the rotor. Elsewhere in the rotor, however, stress distribution remains nearly unchanged, suggesting the component is nearing structural stabilization and becoming less sensitive to added adhesive. On the PM side, the second adhesive layer has a more evident impact. The stress distribution becomes less uniform and harder to interpret, with bending and normal loads now comparable in magnitude and partially overlapping. This indicates a shift from a predominantly bending stress regime (as in layout 1) to a more complex, mixed condition, where the adhesive significantly alters force transmission. In terms of radial deformation, further improvement could be noted compared to layout 2, although less pronounced than in the previous comparison. Quantitatively, from layout 1 to layout 2, deformations have been reduced by 91.31%; from layout 1 to layout 3, the reduction is equal to 93.40%; and finally, from layout 2 to layout 3, deformations have been reduced by 24.07%. Though the first and second comparisons differ only slightly, the direct comparison between layout 2 and layout 3 still shows meaningful gains, confirming the advantage of adding adhesive in reducing peak deformations. As in layout 2, the maximum deformation zone shifts toward the outer regions of the PM, away from the center.

This behavior aligns with the iterative logic: each new adhesive layer is placed where the prior layout showed the highest deformation, helping limit displacements and shifting the deformation peak further. Layout 3 continues the evolutionary improvement from layout 1, offering lower tooth stress, reduced adhesive stress (max 4.27 MPa, considered acceptable), further radial deformation reduction in the PM, and better internal stress redistribution. However, results suggest the system is entering an asymptotic phase, where benefits taper off with each new adhesive layer. To achieve further gains, changes in geometry or materials may be more effective than simply adding more adhesive.

4.4. Layout 4

Layout 4 represents the final configuration, featuring the highest adhesive content. The bonding layer covers nearly the entire contact surface between PM and rotor, except for the ends near the rotor teeth. While effective in reducing adhesive stress, this solution is the least efficient in terms of material usage, requiring a substantial adhesive volume. However, due to the high stiffness of the adhesive film, the contribution of direct PM–tooth contact becomes negligible. This is supported by prior simulations, where increasing the

bonded surface area consistently reduced the load transmitted through PM–tooth contact. The stress distribution of the rotor closely resembles layout 3. Stress levels in the tooth area remain well below critical thresholds, as shown in Figure 11. A detailed comparison of layouts 2, 3, and 4 shows only minor local differences, with nearly identical distributions between layouts 3 and 4. Notably, in this configuration, no mechanical contact between the PM and rotor was activated. The stiffness of the adhesive–rotor system fully supports the centrifugal load. Thus, all force transfer occurs through the adhesive alone. Changes in the PM are more evident. Stress distribution follows a radially increasing trend, from low values at the outer surface to a peak near the rotor. This pattern reflects pure centrifugal loading, where the inner portion of the PM is subjected to the effect of the external mass, resulting in the development of tensile stress fields, while the outer region sees minimal stresses. This gradient suggests an optimal constraint condition enabled by the adhesive, which ensures uniform load sharing and reduces stress concentrations.

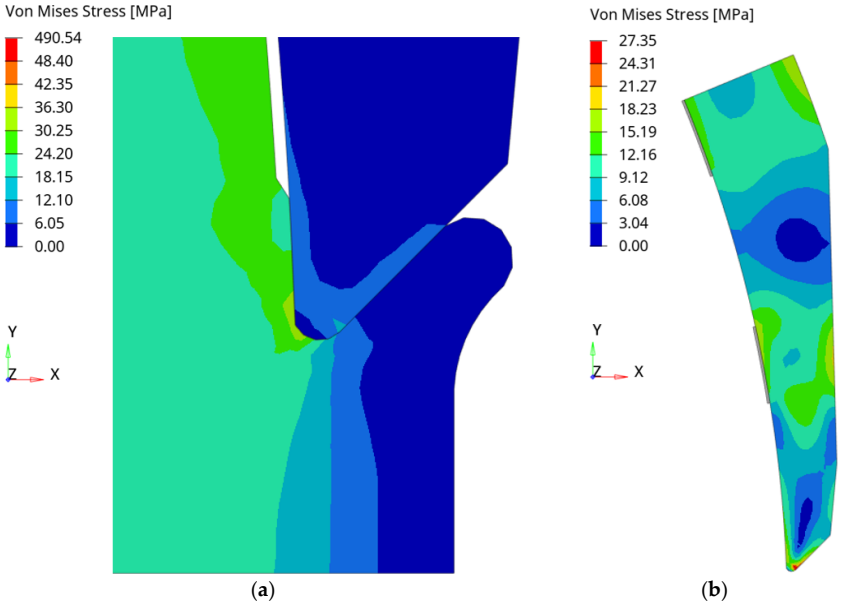

Figure 10. Von Mises stress contour plot—layout 3, (**a**) the stress distribution of the rotor tooth, (**b**) the stress distribution of the PM.

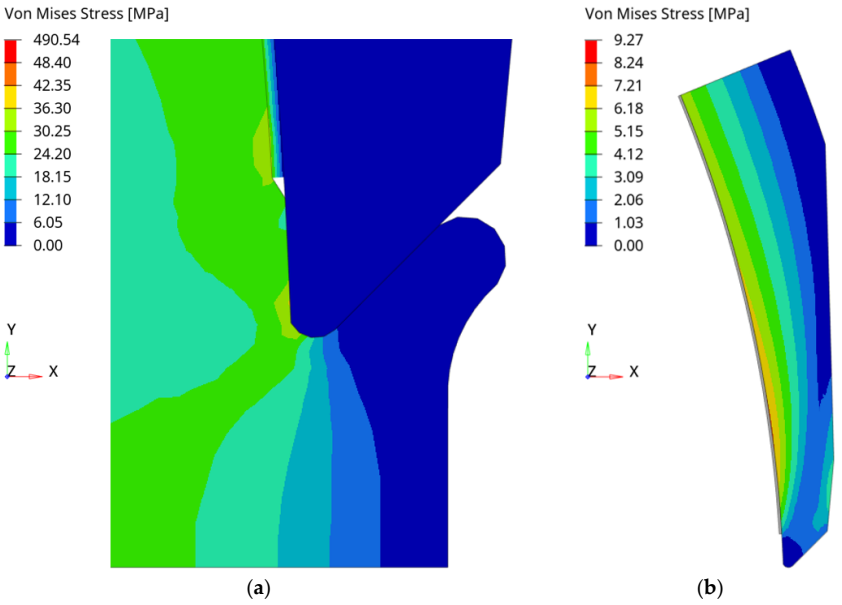

Figure 11. Von Mises stress contour plot—layout 4, (**a**) the stress distribution of the rotor tooth, (**b**) the stress distribution of the PM.

In terms of deformation, layout 4 proves the most effective. The maximum deformation is reduced by 94.57% compared to layout 1 and by ~18% versus layout 3. As in previous cases, increasing the bonded area shifts the maximum deformation zones toward the unbonded PM ends. This consistent behavior confirms a stable and predictable system response. Adhesive stress analysis confirms expectations. Layout 4 achieves the lowest stress levels recorded. The larger bonding surface enables wider load distribution, reducing both peak and average values. Stress ranges from 0.53 MPa to 2.12 MPa, with less pronounced edge effects than in prior layouts, demonstrating the effectiveness of the solution. Overall, layout 4 stands out as the most structurally robust configuration due to its extensive bonded area. However, this robustness comes at the cost of higher adhesive usage and reduced material efficiency. It concludes the simulation series, offering maximum reliability with lower engineering efficiency.

5. Discussion and Conclusions

The analysis of the different bonding configurations between the PM and the rotor has demonstrated that the presence, amount, and spatial distribution of the adhesive were decisive for the mechanical integrity of SPMSM rotors. Increasing the bonded area systematically reduced stress and deformation by shifting the load transfer mechanism from mechanical contact to adhesive-mediated transfer. Across the examined configurations, the maximum PM displacement decreased by up to 94.57%, and the peak adhesive stresses fell from more than 8 MPa to approximately 2 MPa as the bonded surface increased.

These mechanical benefits, however, introduced trade-offs. Although layout 4 provided the lowest stress level and the most homogeneous stress distribution, its practical implementation presented several drawbacks. The wide adhesive cavity required a substantially larger adhesive volume and complicated the dispensing process, increasing the likelihood of voids, incomplete wetting, and variability between units. In addition, quality control became more demanding and the thicker adhesive layer behaved as an additional non-magnetic gap, slightly penalizing electromagnetic performance. For these reasons, layout 4, despite its structural superiority, exhibited low material efficiency and is generally justified only in extreme high-speed or safety-critical applications.

By contrast, layout 3 offered a more favorable balance between structural performance and industrial feasibility. The presence of three smaller adhesive cavities did not increase the complexity of the lamination manufacturing process, but it significantly simplified adhesive application during rotor assembly. Smaller cavities are easier to fill so the risk of air entrapment was reduced. In addition, repeatability was improved and the process was more robust. Moreover, a smaller adhesive volume was required. As a result of this, layout 3 emerged as a technically viable and cost-effective solution for serial manufacturing, especially considering its limited magnetic impact and its lower production cost. In this sense, layout 3 represented the most balanced configuration when considering mechanical robustness, adhesive performance, material usage, and manufacturability.

Several broader design principles might be extracted from the study. Adhesive-bonded retention was effective only when stress transfer occurred over sufficiently large bonded regions. Small bonding interfaces tended to create stress concentration. Hybrid mechanical-adhesive retention, such as dovetail and adhesive architecture considered here, generally provided better stress homogenization and improved safety margins at high speed. Optimal solutions required a balance between mechanical robustness, electromagnetic penalties, and manufacturing constraints. Finally, cohesive-zone-based FEM models were essential for capturing localized adhesive damage mechanisms and stress concentration, which cannot be adequately represented by simplified analytical or lumped structural models.

These findings provided practical guidance for designers of high-speed SPMSMs in sectors such as aerospace, automotive, and high-performance industrial applications. Moderate increases in bonded areas might substantially enhance rotor–PM reliability without resorting to sleeves, thereby avoiding the electromagnetic losses associated with sleeve-induced airgap enlargement. Moreover, adhesive design should be considered a parametric design variable rather than a secondary manufacturing detail, and hybrid retention strategies offer significant benefits under high centrifugal loads.

Overall, the results deliver both configuration-specific insights and generalizable engineering principles for adhesive-based retention in SPMSMs. They provide a solid foundation for more informed rotor–PM interface design and support the development of mechanically robust, electromagnetically efficient, and manufacturable solutions.

Currently, advanced experimental tests are being conducted to determine the actual mechanical strength of the adhesive. The aim of this activity is to develop accurate numerical–experimental correlations. Specifically, these tests will be performed at the average operating temperature of the motor, providing realistic data that closely represents actual service conditions. Additionally, several Finite Element simulations of the experimental tests have been carried out to optimize specimen design. The PM and rotor are subjected to a radially distributed centrifugal force. Since it is extremely challenging to replicate a test in which the rotor experiences the actual centrifugal force, an approximation is adopted. Essentially, the experimental test will consist of a tensile test conducted at a controlled temperature of 120 °C. Once the experimental data are obtained, the FEM model, particularly regarding the adhesive characterization and modeling, will be updated and reassessed.

Another key aspect to evaluate concerns the stress distribution within the adhesive. Figure 12 shows the stress distributions for the three layouts in which the adhesive is present. Consistent with theory and the literature, the edges of the adhesive exhibit higher stress values compared to non-edge regions. Some studies [36,37] suggest combining brittle and ductile adhesives to mitigate these stresses concentrations.

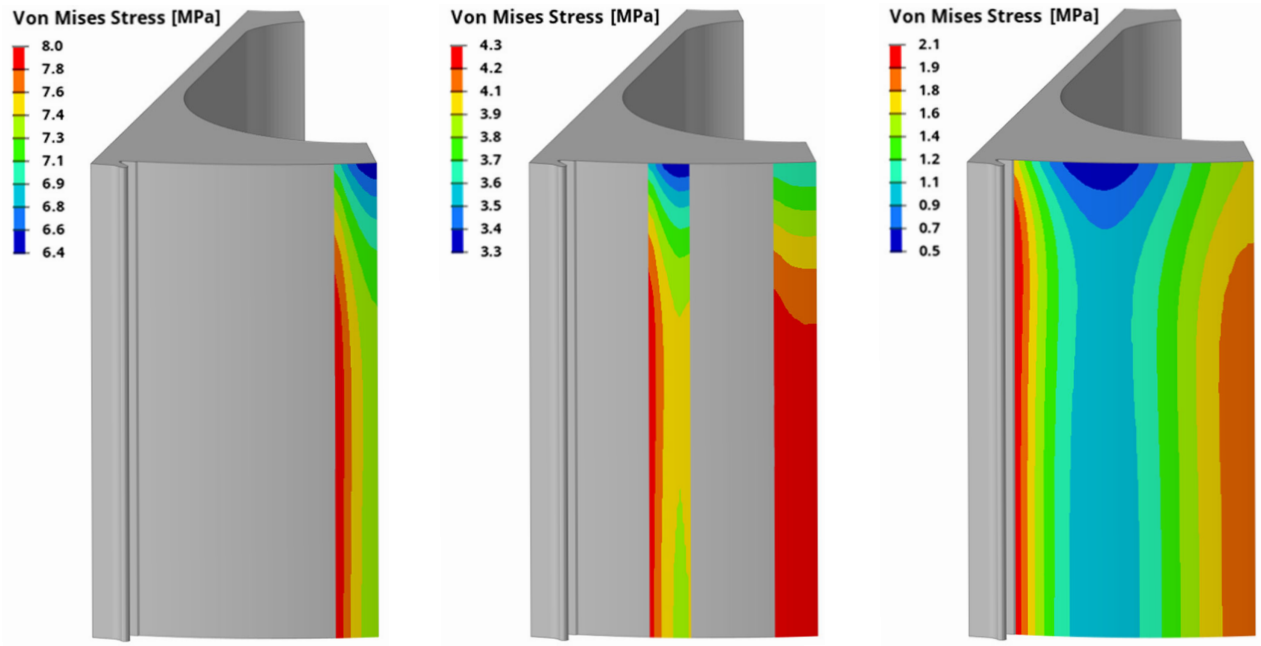

Figure 12. Von Mises stress contour plot for the three different adhesive surface layouts.

However, given the limited size of the bonded sections, such an approach is impractical or, if attempted, extremely complex. The stress distribution shows a recurring pattern

along the left side of the adhesive across the different layouts. While the shape of this pattern is consistent, the stress magnitude decreases with increasing bonded area, but not linearly. In fact, in layouts 2 and 3 at 10,000 rpm, contact between the rotor and PM is observed, whereas no such contact occurs in layout 4. This could explain why the safety factor doubles when moving from layout 2 to 3, where the bonded area increases from 115.4 to 230.8 mm^2, while in the transition from layout 3 to 4, despite tripling the bonded area, the safety factor only doubles.

Finally, Table 4 summarizes the main results obtained in the various configurations analyzed, highlighting the evolution resulting from the optimization of the adhesive distribution between the rotor and the PM. Specifically, the maximum stress and displacement values are reported. The former are reported on the rotor, the adhesive, and the PM. The latter are reported only on the PM.

Table 4. List of the main results.

Layout	1	2	3	4
Max Rotor Stress [MPa]	372.52	54.40	56.84	58.42
Max Ahd. Stress [MPa]	Not present	8.66	4.27	2.12
Max PM Stress [MPa]	182.47	27.35	10.45	9.20
Max PM Displacement [mm]	0.1826	0.0142	0.0107	0.0088
Surface bonded [mm^3]	Not present	115.4	230.8	723.4
Adhesive safety factor	Not present	4.77	9.23	18.78
Torque reduction	0.0%	0.8%	1.0%	3.0%

Author Contributions: Conceptualization, D.O., S.G.B., M.G. (Matteo Giacopini) and M.G. (Michael Galea); Methodology, D.O., M.G. (Matteo Giacopini) and M.G. (Michael Galea); Software, D.O. and G.D.; Validation, D.O.; Formal analysis, D.O.; Investigation, D.O., S.G.B. and G.D.; Data curation, D.O.; Writing—original draft, D.O.; Writing—review & editing, S.G.B., M.G. (Matteo Giacopini) and M.G. (Michael Galea); Visualization, D.O.; Supervision, S.G.B., M.G. (Matteo Giacopini) and M.G. (Michael Galea); Project administration, M.G. (Matteo Giacopini) and M.G. (Michael Galea); Funding acquisition, M.G. (Matteo Giacopini) and M.G. (Michael Galea) All authors have read and agreed to the published version of the manuscript.

Funding: This research was financed by the European Union—Next generation EU trough the "PIANO NAZIONALE DI RIPRESA E RESILIENZA (PNRR) DM352/2022, MISSIONE 4, COMPONENTE 2, INVESTIMENTO 3.3". Astra Research Srl participated in the project as a partner.

Institutional Review Board Statement: Not applicable.

Informed Consent Statement: Not applicable.

Data Availability Statement: The data presented in this study are available on request from the corresponding author due to confidentiality reasons.

Conflicts of Interest: The authors declare that this study received funding from company Astra Research Srl. The funder was not involved in the study design, collection, analysis, interpretation of data, the writing of this article or the decision to submit it for publication.

Abbreviations

The following abbreviations are used in this manuscript:

SPMSM	Surface-mounted Permanent-Magnet Synchronous Machine
FEM	Finite Element Method
EM	Electric Motor
PM	Permanent Magnet

IPMSM	Interior Permanent Magnet Synchronous Machine
Nd-Fe-B	Neodymium–Iron–Boron
CZM	Cohesive Zone Model
SG	Starter Generator
SynRM	Synchronous Reluctance Machine
CPM	Consequent-pole Permanent Magnet
HLRE	Hybrid Low-Rare-Earth

References

1. Guiducci, A.; Barbieri, S.G.; Nuzzo, S.; Batater, D.; Berni, F.; Cicalese, G.; Fontanesi, S.; Franceschini, G. Refined Structural Design and Thermal Analyses of a High-Speed Wound-Field Generator for the More Electrical Aircraft. In Proceedings of the 2023 IEEE Workshop on Electrical Machines Design, Control and Diagnosis (WEMDCD), Newcastle upon Tyne, UK, 13–14 April 2023; pp. 1–6.
2. Puglisi, F.; Barbieri, S.G.; Mantovani, S.; Devito, G.; Nuzzo, S. Multi-Physics and Multi-Objective Optimization of a Permanent Magnet-Assisted Synchronous Reluctance Machine for Traction Applications. *Proc. Inst. Mech. Eng. C J. Mech. Eng. Sci.* **2024**, *238*, 7945–7962. [CrossRef]
3. Wang, S.-C.; Nien, Y.-C.; Huang, S.-M. Multi-Objective Optimization Design and Analysis of V-Shape Permanent Magnet Synchronous Motor. *Energies* **2022**, *15*, 3496. [CrossRef]
4. Hiruma, S.; Ohtani, M.; Soma, S.; Kubota, Y.; Igarashi, H. Novel Hybridization of Parameter and Topology Optimizations: Application to Permanent Magnet Motor. *IEEE Trans. Magn.* **2021**, *57*, 1–4. [CrossRef]
5. Yoon, K.-Y.; Baek, S.-W. Torque Ripple Reduction and Efficiency Enhancement of Flared-Type Consequent-Pole Motors via Asymmetric Air-Gap and Structural Optimization. *Appl. Sci.* **2025**, *15*, 11520. [CrossRef]
6. Yoon, K.; You, Y. Optimal Design of a Novel Consequent-Pole Interior Permanent Magnet Motor with Flared-Structured Rotor. *Appl. Sci.* **2024**, *14*, 1496. [CrossRef]
7. Poudel, B.; Amiri, E.; Rastgoufard, P.; Mirafzal, B. Toward Less Rare-Earth Permanent Magnet in Electric Machines: A Review. *IEEE Trans. Magn.* **2021**, *57*, 1–19. [CrossRef]
8. Wang, Z.; Wang, X.; Bao, X. A PM Dimensions Design Method for Hybrid Less Rare-Earth Permanent Magnet Motors Based on Analytical Approach. *IEEE Trans. Transp. Electrif.* **2025**, *11*, 6512–6524. [CrossRef]
9. Zhu, X.; Zhao, M.; Wang, H.; Shen, Y.; Zhou, Y.; He, Y.; Lee, C.H.T. Design and Investigation of Flux-Reversal Permanent-Magnet Motor with Less Rare-Earth Magnet for Low-Cost Application. *IEEE Trans. Transp. Electrif.* **2025**, *11*, 4133–4144. [CrossRef]
10. Rivera, C.A.; Ugalde, G.; Poza, J.; Garramiola, F.; Badiola, X. Less Rare-Earth Electromagnetic Design for a High-Performance Permanent Magnet Motor. *Appl. Sci.* **2022**, *12*, 3736. [CrossRef]
11. Devito, G.; Theofanous, A.; Galea, M.; Barater, D.; Nuzzo, S. Design Optimization of a Starter Generator for More Sustainable High Power Density Aerospace Applications. In Proceedings of the IECON 2024—50th Annual Conference of the IEEE Industrial Electronics Society, Chicago, IL, USA, 3 November 2024; pp. 1–6.
12. Yoon, K.Y.; Lee, S.T. Performance Improvement of Permanent-Magnet-Synchronous Motors through Rotor Shape Optimization of Marine Blowing System with High-Speed Rotation. *Energies* **2023**, *16*, 5486. [CrossRef]
13. Park, J.H.; Lee, J.G.; Hong, D.K. A Comparative Study of Rotor Topology of PMSM for Podded Propulsion in Marine Applications. *J. Electr. Eng. Technol.* **2025**, *20*, 4115–4134. [CrossRef]
14. Owusu, D.; Amuzuvi, C.; Attachie, J. Vibration-Induced Thermal Fault Analysis and Optimisation of Induction Motors Using Artificial Intelligence. *Am. J. Artif. Intell.* **2025**, *9*, 91–106. [CrossRef]
15. Aguebor, O. Electric Motor Faults: For Power System Protection. *Power Syst. Prot.* **2023**. [CrossRef]
16. Popsi, N.R.S.; Anik, A.; Verma, R.; Viana, C.; Iyer, K.L.V.; Kar, N.C. Influence of Electric Motor Manufacturing Tolerances on End-of-Line Testing: A Review. *Energies* **2024**, *17*, 1913. [CrossRef]
17. Vagati, A.; Pellegrino, G.; Guglielmi, P. Comparison Between SPM and IPM Motor Drives for EV Application. In Proceedings of the XIX International Conference on Electrical Machines—ICEM 2010, Rome, Italy, 6–8 September 2010; pp. 1–6.
18. Lalana, E.H. Permanent Magnets and Its Production by Powder Metallurgy. *Rev. Metal.* **2018**, *54*, e121.
19. Cui, J.; Ormerod, J.; Parker, D.; Ott, R.; Palasyuk, A.; Mccall, S.; Paranthaman, M.P.; Kesler, M.S.; McGuire, M.A.; Nlebedim, I.C.; et al. Manufacturing Processes for Permanent Magnets: Part I—Sintering and Casting. *JOM* **2022**, *74*, 1279–1295. [CrossRef]
20. Takagi, K.; Hirayama, Y.; Okada, S.; Yamaguchi, W.; Ozaki, K. Novel Powder Processing Technologies for Production of Rare-Earth Permanent Magnets. *Sci. Technol. Adv. Mater.* **2021**, *22*, 150–159. [CrossRef]
21. Rabinovich, Y.M.; Sergeev, V.V.; Maystrenko, A.D.; Kulakovsky, V.; Szymura, S.; Bala, H. Physical and Mechanical Properties of Sintered Nd-Fe-B Type Permanent Magnets. *Intermetallics* **1996**, *4*, 641–645. [CrossRef]

22. Cho, H.; Jang, S. A Design Approach to Reduce Rotor Losses in High-Speed Permanent Magnet Machine for Turbo-Compressor. In Proceedings of the 2006 IEEE International Magnetics Conference (INTERMAG), San Diego, CA, USA, 8–12 May 2006; p. 209.
23. Bianchi, N.; Bolognani, S.; Luise, F. Potentials and Limits of High-Speed PM Motors. *IEEE Trans. Ind. Appl.* **2004**, *40*, 1570–1578. [CrossRef]
24. Zubkov, Y.; Makarichev, Y.; Alimbekov, M. How Permanent Magnets Bonding Methods Affect the Rotor Mechanical Strength in an SPM Synchronous Starter. In Proceedings of the 2019 International Conference on Industrial Engineering, Applications and Manufacturing (ICIEAM), Sochi, Russia, 25–29 March 2019; pp. 1–5.
25. Xing, Z.; Wang, X.; Zhao, W. Design and Analysis of Basic Model of High-Speed Surface-Mounted Permanent Magnet Synchronous Motors Based on Subdomain Method. *J. Electr. Eng. Technol.* **2023**, *18*, 3635–3646. [CrossRef]
26. Gobbi, M.; Sattar, A.; Palazzetti, R.; Mastinu, G. Traction Motors for Electric Vehicles: Maximization of Mechanical Efficiency—A Review. *Appl. Energy* **2024**, *357*, 122496. [CrossRef]
27. G, V.; Chandrakala, K.R.M.V.; Kumari, P.; Saravanan, S.; Balamurugan, S.; P, R. Enhanced Power Density and Energy-Efficient High-Speed Permanent Magnet Starter-Generator Using Multi-Physics Optimization Strategies for Future Electric Aircraft. *Results Eng.* **2025**, *28*, 107216. [CrossRef]
28. Tun, Z.M.; Seangwong, P.; Fernando, N.; Siritaratiwat, A.; Khunkitti, P. Power Generation Enhancement of Surface-Mounted Permanent Magnet Wind Generators Using Eccentric Halbach Array Permanent Magnets. *Sustainability* **2025**, *17*, 5893. [CrossRef]
29. Hekmati, A.; Mahalli, I.S. A Comprehensive Review on High Speed Permanent Magnet Motors and Their Modern Applications. *Electromech. Energy Convers. Syst.* **2021**, *1*, 61–67.
30. Du, G.; Li, N.; Zhou, Q.; Gao, W.; Wang, L.; Pu, T. Multi-Physics Comparison of Surface-Mounted and Interior Permanent Magnet Synchronous Motor for High-Speed Applications. *Machines* **2022**, *10*, 700. [CrossRef]
31. Elices, M.; Guinea, G.V.; Gómez, J.; Planas, J. The Cohesive Zone Model: Advantages, Limitations and Challenges. *Eng. Fract. Mech.* **2002**, *69*, 137–163. [CrossRef]
32. Campilho, R.D.S.G.; Banea, M.D.; Neto, J.A.B.P.; Da Silva, L.F.M. Modelling Adhesive Joints with Cohesive Zone Models: Effect of the Cohesive Law Shape of the Adhesive Layer. *Int. J. Adhes. Adhes.* **2013**, *44*, 48–56. [CrossRef]
33. Shahverdi, M.; Vassilopoulos, A.P.; Keller, T. Modeling Effects of Asymmetry and Fiber Bridging on Mode I Fracture Behavior of Bonded Pultruded Composite Joints. *Eng. Fract. Mech.* **2013**, *99*, 335–348. [CrossRef]
34. Campilho, R.D.S.G.; Banea, M.D.; Pinto, A.M.G.; Da Silva, L.F.M.; De Jesus, A.M.P. Strength Prediction of Single- and Double-Lap Joints by Standard and Extended Finite Element Modelling. *Int. J. Adhes. Adhes.* **2011**, *31*, 363–372. [CrossRef]
35. Ismagilov, F.R.; Vavilov, V.E. Optimization of a High-Temperature Starter—Generator of Inverted Design for Aircraft. *Russ. Electr. Eng.* **2019**, *90*, 391–396. [CrossRef]
36. da Silva, L.F.M.; Lopes, M.J.C.Q. Joint Strength Optimization by the Mixed-Adhesive Technique. *Int. J. Adhes. Adhes.* **2009**, *29*, 509–514. [CrossRef]
37. Silva, M.R.G.; Marques, E.A.S.; da Silva, L.F.M. Behaviour Under Impact of Mixed Adhesive Joints for the Automotive Industry. *Lat. Am. J. Solids Struct.* **2016**, *13*, 835–853. [CrossRef]